Check for updates

Proceedings of the ASME 2024 19th International Manufacturing Science and Engineering Conference
MSEC2024
June 17-21, 2024, Knoxville, Tennessee

MSEC2024-124375

Downloaded from http://asmedigitalcollection.asme.org/MSEC/proceedings-pdf/MSEC2024/88117/V002T06A008/7366697/v002t06a008-msec2024-124375.pdf by University of Michigan user on 26 January 2025

NUMERICAL ANALYSIS OF THE MELT POOL KINETICS IN SELECTIVE LASER MELTING BASED ADDITIVE MANUFACTURING OF THERMOELECTRIC POWDERS

Jagannath Suresh[1], Gagan K Goyal[2,*], Haozheng Wang[2], Lei Zuo[2,*],

[1]Department of Mechanical Engineering, Virginia Tech, Blacksburg, VA
[2]Department of Naval Architecture and Marine Engineering, University of Michigan, Ann Arbor, MI

ABSTRACT

Thermoelectric generators convert heat energy to electricity and can be used for waste heat recovery, enabling sustainable development. Selective Laser Melting (SLM) based additive manufacturing process is a scalable and flexible method that has shown promising results in manufacturing high zT Bi_2Te_3 material and is possible to be extended to other material classes such as Mg_2Si. The physical phenomena of melting and solidification were investigated for SLM-based manufacturing of thermoelectric (Mg_2Si) powders through comprehensive numerical models developed in MATLAB. In this study, Computational Fluid Dynamics (CFD)-based techniques were employed to solve conservation equations, enabling a detailed understanding of temperature evolution within the molten pool. This approach was critical for optimizing processing parameters in our investigation, which were also used for printing the Mg_2Si powders using SLM. Additionally, a phase field-based model was developed to simulate the directional solidification of the Mg_2Si in MATLAB. Microstructural parameters were studied to correlate the effects of processing parameters to the microstructure of Mg_2Si.

Keywords: Additive Manufacturing, Thermoelectrics, Phase Field, CFD

1. INTRODUCTION

Selective laser melting (SLM), a powder bed fusion technology, involves the use of a laser to selectively melt and fuse metallic powder particles layer by layer. This process may produce parts with intricate designs and high mechanical strength, making it ideal for applications in aerospace, and automotive industries[1].

Thermoelectric (TE) materials convert heat into electricity, and have seen limited advancements through additive manufacturing techniques. Thimont et al.[2] have highlighted the possibility of TE generators (TEGs) featuring leg designs. Mid-temperature (573-723K) application range TE materials such as Mg_2Si have seen significant progress in material and device development,[3–5], although the application of laser manufacturing methods has not been tested yet. Zhang et al. [6] investigated the thermal spraying of Mg_2Si and discovered that the point defects resulting from the high quench rate contributed to an increased ZT value. Although, controlling the non-equilibrium synthesis conditions in SLM, especially with high vapor pressure element Mg is challenging. Hence, an assessment of the processing conditions and their relation with the material properties is necessary to identify the suitable laser parameters. Li et al. [7] conducted studies on the growth patterns of Mg_2Si particles in Mg_2Si/Al composites. They concluded that the ultimate shape of the Mg_2Si crystals is influenced by both their inherent crystal structure and the conditions under which they grow.

To understand the thermal changes in SLM, the expanded model by Xiao et al.[8] analyzed a single-component metal powder bed in SLM, dividing the melting process into different stages accounting for shrinkage and gas volume fraction effects. Wu et al.[9] used a similar approach to model the meltpool dynamics to manufacture Mg_2Si powders with SLM.

Different numerical methods have been used to simulate the dendritic growth during solidification. Phase field [10] methods are the most prevalent techniques for modeling dendrite growth during solidification. The phase field method is built on using continuous field variables to model the evolution of microstructures, like phase transitions and interface dynamics, in a diffuse interface framework. Tian et al. [10] utilized a two-dimensional phase field model to simulate dendritic solidification in magnesium alloys. Additionally, Wang et al.[11] used the CALPHAD database inputs to examine the growth behavior of the Mg_2Si intermetallic layer in Mg infiltrated Si-foams. Despite these advancements, challenges remain in the SLM process of thermoelectric Mg_2Si powders.

This study aims to bridge this gap by presenting a detailed numerical analysis of melt pool kinetics in the SLM of thermoelectric powders, focusing on the melting and solidification pro-

*Corresponding author
Documentation for `asmeconf.cls`: Version 1.34, March 21, 2024.

Copyright © 2024 by ASME

cess to refine the process parameters for the SLM fabrication of Mg_2Si. This paper is organized as follows. In section 2, we present the mathematical model used for developing the CFD-based melting dynamics and the phase field-based solidification dynamics. In section 3, we describe the numerical results, along with the optimized process parameters identified through the analysis.

2. MATHEMATICAL MODEL

2.1 Computational Fluid Dynamics Based Thermal Model

2.1.1 Physical Model. A Computational Fluid Dynamics model was developed to simulate the melt pool dynamics and obtain the temperature distribution during the fabrication of Mg_2Si using SLM. Fig. 1 depicts the manufacturing procedure utilized in the process. A Gaussian laser beam moving in the x direction at speed U_b is employed to melt the metal powders. The size

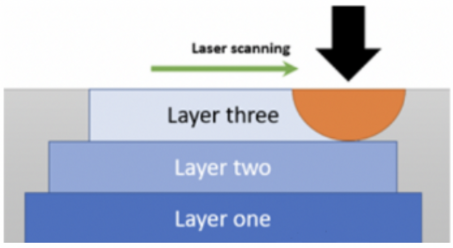

FIGURE 1: SLM PROCESS

of the computational domain is chosen to be 3.6 mm x 1.2 mm x 1.2 mm, which is significantly larger than the laser spot size and, hence, the molten pool. Hence, the temperature fluctuation farther away from the molten pool was assumed to be very small. The molten pool was assumed to be symmetric, and hence, only half the molten pool was modeled to reduce the computational time.

2.1.2 Governing Equations. A one-phase model [12], was used for the modeling. Since the molten pool moves along with the laser beam, the problem is modeled in a moving reference frame with the domain moving at a velocity U_b. A few assumptions were taken to simplify the problem:

1. The porosity of the powder bed was assumed to be uniform. Throughout the melting phase, the gas within the porous structure was gradually displaced as a result of the pressure exerted by the liquid. Ultimately, both the liquid and sintered regions completely expelled the gas.
2. The Boussinesq approximation [13] was implemented in the Z direction to account for the buoyancy-driven flow and also reduce the computational expense.
3. The material has constant thermophysical properties, including the viscosity, specific heat, and thermal conductivity in each phase, and the variation in values during phase change is calculated with a weighted approach.
4. The model is developed for a single raster trajectory in the X-direction on the powder bed.

The governing equations were adapted to a unified single-phase model for all areas within the computational domain within a coordinate system in motion as follows:

- Continuity Equation

$$\frac{\partial \rho}{\partial t} + \frac{\partial(\rho(u-u_b))}{\partial x} + \frac{\partial(\rho v)}{\partial y} + \frac{\partial(\rho w)}{\partial z} \quad (1)$$

- X-Momentum Equation

$$\frac{\partial(\rho u)}{\partial t} + \frac{\partial(\rho u(u-u_b))}{\partial x} + \frac{\partial(\rho uv)}{\partial y} + \frac{\partial(\rho uw)}{\partial z} = -\frac{\partial P}{\partial x} + \frac{\partial}{\partial x}\left(\frac{\mu^+ \partial u}{\partial x}\right) + \frac{\partial}{\partial y}\left(\frac{\mu^+ \partial u}{\partial y}\right) + \frac{\partial}{\partial z}\left(\frac{\mu^+ \partial u}{\partial z}\right) \quad (2)$$

- Y-Momentum Equation

$$\frac{\partial(\rho v)}{\partial t} + \frac{\partial(\rho v(u-u_b))}{\partial x} + \frac{\partial(\rho vv)}{\partial y} + \frac{\partial(\rho vw)}{\partial z} = -\frac{\partial P}{\partial y} + \frac{\partial}{\partial x}\left(\frac{\mu^+ \partial v}{\partial x}\right) + \frac{\partial}{\partial y}\left(\frac{\mu^+ \partial v}{\partial y}\right) + \frac{\partial}{\partial z}\left(\frac{\mu^+ \partial v}{\partial z}\right) \quad (3)$$

- Z-Momentum Equation

$$\frac{\partial(\rho w)}{\partial t} + \frac{\partial(\rho w(u-u_b))}{\partial x} + \frac{\partial(\rho wv)}{\partial y} + \frac{\partial(\rho ww)}{\partial z} = -\frac{\partial P}{\partial z} + \frac{\partial}{\partial x}\left(\frac{\mu^+ \partial w}{\partial x}\right) + \frac{\partial}{\partial y}\left(\frac{\mu^+ \partial w}{\partial y}\right) + \frac{\partial}{\partial z}\left(\frac{\mu^+ \partial w}{\partial z}\right) + \rho g_r (T - T_e)(\beta_T + \beta_s C_s) \quad (4)$$

- Energy Equation

$$\frac{\partial(\rho h)}{\partial t} + \frac{\partial(\rho h(u-u_b))}{\partial x} + \frac{\partial(\rho hv)}{\partial y} + \frac{\partial(\rho hw)}{\partial z} = \frac{\partial}{\partial x}\left(\frac{k^+ \partial T}{\partial x}\right) + \frac{\partial}{\partial y}\left(\frac{k^+ \partial T}{\partial y}\right) + \frac{\partial}{\partial z}\left(\frac{k^+ \partial T}{\partial z}\right) + S_h \quad (5)$$

The last term in Eq. 4 is the Boussinesq approximation term that accounts for the buoyancy in the molten pool, which is a volume effect. The source term S_h in Eq. 5 was used to model the enthalpy change during phase transition.

The powders were assumed to start melting at a temperature T_M - Δ T (Δ T = 200K) and completely melt at the melting temperature T_M. Hence, the mass fraction of liquid was defined separately in these temperature intervals as follows:

$$f_l = \begin{cases} 1 & T \geq T_M \\ \frac{T_M - T}{\Delta T} & T_M - \Delta T < T < T_M \\ 0 & T \leq T_M - \Delta T \end{cases} \quad (6)$$

The fraction of solid powders in the mushy region is given by:

$$f_s = 1 - f_l \quad (7)$$

The effective thermal conductivity (k_{eff}) of the packed powder bed was calculated using the empirical correlation proposed by Hadley [14] and also outlined by Xiao et al.[8].

The effective thermal conductivity and effective viscosity in the melting mushy zone were calculated by taking a summation of the properties of the solid powders and the melted liquid weighted by their corresponding mass fractions as follows:

$$\mu^+ = \mu_s f_s + \mu_l f_l \quad (8)$$

$$k^+ = k_{eff} f_s + k_l f_l \quad (9)$$

Downloaded from http://asmedigitalcollection.asme.org/MSEC/proceedings-pdf/MSEC2024/88117/V002T06A008/7366697/v002t06a008-msec2024-124375.pdf by University of Michigan user on 26 January 2025

Copyright © 2024 by ASME

The enthalpy of the powder was assumed to be temperature dependent and was calculated by:

$$h = \int_0^T c_{ps} dT \tag{10}$$

The enthalpy change during phase transition was dependent on the thermal capacity and the latent heat, which was given by:

$$\delta H = [\int_0^T (c_{pl} - c_{ps}) dT + L] f_l \tag{11}$$

Since the thermal capacity of the sintered material remained constant during the fabrication, the enthalpy change was further simplified as:

$$\delta H = \begin{cases} L & T \geq T_M \\ L f_l & T_M - \Delta T < T < T_M \\ 0 & T \leq T_M - \Delta T \end{cases} \tag{12}$$

Finally, the source term S_h in the energy equation consisted of transient and convective terms and was calculated as taken in ref. [12] as follows:

$$S_h = -\frac{\partial}{\partial t}(\rho \delta H) - \frac{\partial}{\partial x}(\rho(u-u_b)\delta H) - \frac{\partial}{\partial y}(\rho v \delta H) - \frac{\partial}{\partial z}(\rho w \delta H) \tag{13}$$

2.1.3 Boundary Conditions. Boundary conditions are defined on each face of the given computational domain as follows:

- **Boundary A**(Top face of the domain in Fig. 2): Heat transfer balance was done on this boundary as the temperature boundary condition. Part of the heat absorbed by the powder bed from the Gaussian laser beam was lost to the environment through convection and radiation. Part of the heat was also conducted into the powder bed. The values of the convective heat transfer coefficient and emissivity were taken from literature [15, 16]. The condition is implemented as follows:

$$-k_{eff} \frac{\partial T}{\partial z}_{z=s} = \theta q_{laser} + h_c(T - T_a) + \epsilon_b \sigma_b (T^4 - {T_a}^4) \tag{14}$$

where,

$$\theta = \begin{cases} 1 & \text{Laser spot} \\ 0 & \text{Rest of the area} \end{cases} \tag{15}$$

The heat flux of the Gaussian laser beam is given as follows:

$$q_{laser} = -\frac{q_o}{\pi R^2} \exp\left\{(-\frac{r^2}{R^2})\right\} \tag{16}$$

The shear force and surface tension were assumed to be balanced at the top surface for the velocity boundary condition as follows:

$$\mu^+(\frac{\partial v_s}{\partial n} + \frac{\partial v_n}{\partial s}) = \frac{\partial \sigma}{\partial T}\frac{\partial T}{\partial s} \tag{17}$$

Where v_s and v_n are tangential and normal velocity components at the heating surface.

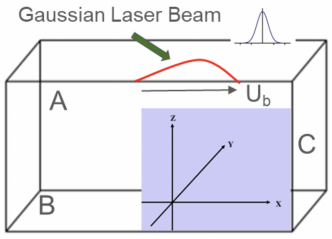

FIGURE 2: COMPUTATIONAL DOMAIN

- **Boundary B**(Front face of the domain in Fig. 2): This face is symmetrical, and hence symmetry boundary conditions are applied here as follows:

$$\frac{\partial T}{\partial y}_{y=0} = 0 \tag{18}$$

$$\frac{\partial u}{\partial y}_{y=0} = \frac{\partial w}{\partial y}_{y=0} = v_{y=0} = 0 \tag{19}$$

- **Boundary C**(Right, left, and bottom faces of the domain in Fig. 2): The right, left, and bottom boundaries were far from the laser spot due to the size of the computational domain, and since the thermal conductivity of the material was small, the temperature on these faces were assumed to be constant at the ambient temperature:

$$T = T_a \tag{20}$$

The velocities on these boundaries were assumed to be zero as there was no particle motion away from the melt pool.

$$u = v = w = 0 \tag{21}$$

2.1.4 Numerical Procedures. The simulated case is a quasi-steady state, three-dimensional, non-linear problem. A false transient method is used to solve the problem, and a steady state is said to be obtained when the temperature and velocity distribution do not change with time. A Finite Volume-based approach was employed by dividing the domain into multiple control volumes and solving the governing equations in each control volume. The SIMPLER algorithm proposed by Patankar [17] was used to solve the governing equations 1-5. The equations were discretized using the Total Variation Diminishing (TVD) Scheme proposed by Van Leer [18] as it's second-order accurate and unconditionally stable without overshoot as used in reference [9]. The flux limiter function used in this scheme is given by:

$$\psi(r) = \frac{r + |r|}{1 + r^2} \tag{22}$$

The above limiter function is chosen so that the denominator is never zero, hence making the simulation stable.
The discretization for the 3D cartesian grid system was adapted from the 2D scheme described by Versteeg et al. [19] as:

$$a_P \phi_P = a_W \phi_W + a_E \phi_E + a_S \phi_S + a_N \phi_N + a_F \phi_F + a_B \phi_B + {S_u}^{DC} + S_\phi \tag{23}$$

Downloaded from http://asmedigitalcollection.asme.org/MSEC/proceedings-pdf/MSEC2024/88117/V002T06A008/7366697/v002t06a008-msec2024-124375.pdf by University of Michigan user on 26 January 2025

Copyright © 2024 by ASME

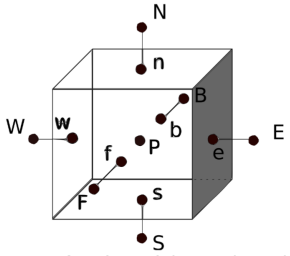

FIGURE 3: A SINGLE CONTROL VOLUME

Where the superscripts W, E, S, N, F, and B are the West, East, South, North, Front, and Back faces of the control volume, respectively, as shown in Fig. 3.

vspace-12mm The coefficient a_P is given by:

$$a_P = a_W + a_E + a_S + a_N + a_F + a_B + (F_e - F_w) + (F_n - F_s) + (F_b - F_f) \quad (24)$$

where the deferred correction source term ${S_u}^{DC}$ is computed for the TVD scheme as given in ref. [19].

Uniformly structured hexahedron grids, $150 \times 75 \times 75$ in the X, Y, and Z directions were adopted for the modeling. The false time step was set to 0.0001s to ensure the fulfillment of the CFL condition for numerical stability. The inner iterative process persisted until the residuals of all governing equations reached a value below 10^{-5}. The solution was assumed to be converged when $|\frac{\phi_N - \phi_{N-1}}{\phi_N}| < 10^{-3}$. The Alternating Direction Implicit solver was used to solve the equations, and the Block Correction Method was used to accelerate the convergence as employed in [9]. The complete code was developed in MATLAB.

2.1.5 Material Properties. The thermal conductivity values of Mg_2Si in the solid and liquid phase were defined according to the measured values of Mg_2Si thermal conductivity in a wide temperature range [20–22]. It is to be noted that the thermal conductivity values of these powders decrease with the increase in temperature, and hence, the liquid and solid thermal conductivities were approximated accordingly after sufficient testing. The sintering temperature of Mg_2Si is known to be in the range of 850°C - 900°C [23] and is set at (1173K)900°C for this study. Further, the melting point of bulk Mg_2Si is known to be 1375K [24]. Hence, a few initial tests were run by setting the sintering temperature to 1375K and were tested experimentally, as discussed in Section 3. All the material properties and input parameters used for the final simulation are listed in Table 1.

2.2 Phase Field Model

2.2.1 Governing Equations. This study employed a phase field-based approach to simulate the microstructure growth of Mg_2Si in SLM. The phase field order parameter, a key component in the simulation, dynamically evolves based on the governing equations of the phase field, which are intricately coupled with the heat and solute diffusion equations. The simulation methodology followed a directional solidification of dilute binary alloys approach, introducing a smooth yet rapid variation in the order parameter value at the interface developed by Echebarria et al. [25]. A notable inclusion in the model was a corrective anti-trapping current strategically implemented to counterbalance the

TABLE 1: SIMULATION PARAMETERS - CFD

Input	Value	Unit
Specific heat (c_p)	67.87[24]	$Jkg^{-1}K^{-1}$
Solid thermal conductivity (k_p)	5[20–22]	$Wm^{-1}K^{-1}$
Liquid thermal conductivity (k_l)	3.5[20–22]	$Wm^{-1}K^{-1}$
Gas thermal conductivity (k_g)	0.024[14]	$Wm^{-1}K^{-1}$
Porosity (ϵ)	0.2	
Density (ρ)	1990[24]	kgm^{-3}
Liquid viscosity (μ_l)	5×10^{-3}[24]	$kgm^{-1}s^{-1}$
Solid viscosity (μ_s)	1×10^{4}[8]	$kgm^{-1}s^{-1}$
Latent heat (L)	4.5×10^{5}[24]	Jkg^{-1}
Sintering temperature (T_M)	900[23]	°C
Thermal expansion coeff. (β_T)	1.1×10^{-5}[24]	K^{-1}
Ambient temperature (T_a)	298.15	K
Convective heat transfer coeff.(h_c)	10[8]	$Wm^{-2}K^{-1}$
Laser diameter (R)	0.2	mm
Laser power (Q)	10-15	W
Scanning speed (u_b)	0.05-0.2	ms^{-1}
Boltzmann constant (σ_b)	5.67×10^{-8}	$Wm^{-2}K^{-4}$
$\partial\sigma/\partial T$	-10^{-5}[8]	$kgs^{-2}K$
Radiation emissivity (ϵ_b)	0.86[9]	

spurious solute trapping associated with the abrupt jump of chemical potential across the interface [26]. A few assumptions were considered for the formulation of the phase field model [27]:

1. The effect of convection in the liquid is assumed to be negligible, and the mass transport is assumed to be entirely governed by diffusion.
2. The effect of Latent heat of fusion is neglected by imposing the temperature field in the form of a temperature gradient.
3. Thermophysical properties are considered to be constants.
4. Solute diffusivity in the solid is 2 orders of magnitude less than the solute diffusivity in the liquid. So, the solute diffusivity in the solid state is neglected.
5. Solid-liquid interface is considered to be in local equilibrium.

The constitutive equations for the model were chosen as Eq.(68) and Eq.(69) from the reference [25]. By using the phase field variables [28], the dimensionless form of the governing equations for the phase field order parameter and the concentration variable in 2 dimensions is given by:

$$\left[1 - (1-k)\frac{x - \tilde{V}_P t}{\tilde{l}_T}\right](a_s(\theta))^2 \frac{\partial \phi}{\partial t} = \boldsymbol{\nabla} \cdot \left((a_s(\theta))^2 \boldsymbol{\nabla} \cdot \phi\right) + \sum_{m=x,y} \left[\partial_m(|\boldsymbol{\nabla} \cdot \phi|^2) a_s(\theta) \frac{\partial a_s(\theta)}{\partial(\partial_m \phi)}\right] + \phi - \phi^3 - \lambda(1-\phi^2)^2 \left(U + \frac{x - \tilde{V}_P t}{\tilde{l}_T}\right) \quad (25)$$

Downloaded from http://asmedigitalcollection.asme.org/MSEC/proceedings-pdf/MSEC2024/88117/V002T06A008/7366697/v002t06a008-msec2024-124375.pdf by University of Michigan user on 26 January 2025

Copyright © 2024 by ASME

$$\left(\frac{1+k}{2}-\frac{1-k}{2}\phi\right)\frac{\partial U}{\partial t}=\nabla\cdot\left(\tilde{D}\frac{1-\phi}{2}\nabla\cdot U+\frac{1}{2\sqrt{2}}\left[1+(1-k)U\right]\frac{\partial\phi}{\partial t}\frac{\nabla\cdot\phi}{|\nabla\cdot\phi|}\right)+\left(1+(1-k)U\right)\frac{1}{2}\frac{\partial\phi}{\partial t} \quad (26)$$

with

$$U=\frac{1}{1-k}\left[\frac{\frac{c}{c_l{}^o}}{\frac{(1-\phi)}{2}+k\frac{(1+\phi)}{2}}-1\right] \quad (27)$$

where ϕ is the phase field order parameter (ϕ = 1 in solid, and ϕ = -1 in liquid) U is the generalized dimensionless supersaturation, c is the solute concentration field, and $c_l{}^o = \frac{c_\infty}{k}$ is the solute concentration of a flat interface at a reference (Solidus) temperature T_o for an alloy of solute concentration c_∞, and a solute partition coefficient k [29]. Space is taken in the units of the interfacial width W, and time in the units of the relaxation time τ_o [25]. The non-dimensionalized values $\tilde{D}$, $\tilde{V}_P$, and $\tilde{l}_T$ are calculated as referenced in [25].

And, the coupling constant λ should be sufficiently small to ensure the convergence of the simulation while avoiding unnecessary computational expenses [30].

$$\lambda = a_1\frac{W}{d_o} \quad (28)$$

The thermal length l_T is:

$$l_T=\frac{|m|c_\infty(\frac{1}{k}-1)}{G} \quad (29)$$

The capillary length d_o is given by:

$$d_o=\frac{\Gamma}{\left[|m|c_\infty(\frac{1}{k}-1)\right]} \quad (30)$$

with Γ the Gibbs Thomson coefficient of the solid-liquid interface, where a_1 = 0.8839, and a_2 = 0.6267. The relaxation time τ_o is:

$$\tau_o=\frac{a_2\lambda W^2}{D} \quad (31)$$

The surface tension anisotropy is taken to be a four-fold anisotropy as taken in the reference [27, 29] and is given by:

$$a_s(\bar{\theta})=1+\epsilon_4\cos(4\bar{\theta}) \quad (32)$$

where ϵ_4 is the strength of anisotropy and $\bar{\theta}$ is the angle between the normal to the interface and a fixed crystalline axis. The detailed discretization and development of Eq. (25) and Eq. (26) are taken from Appendices B and C in ref. [29].

2.2.2 Implementation. The phase field Eq. (25), and Eq. (26), are discretized and solved using the Finite Difference Method on a grid of square elements with spacing ΔX. The Euler explicit scheme is used to march ahead in time with a time step Δt. For the Laplacian of the phase field, a standard five-point stencil is used with a maximally isotropic discretization as mentioned in Appendix B of the reference [25].

The first and second terms on the right-hand side of Eq.(25) involving anisotropy are solved by converting them into first and second-order spatial derivatives of ϕ as depicted in Appendix B of the reference [29]. The first and second terms on the right-hand side of Eq. (26) are the terms accounting for the liquid diffusion and the anti-trapping current (developed by Echebarria et al. [25]) respectively and are developed as per the formulation given in Appendix C of the reference [29].

The calculations in the bulk phase are reduced by calculating the anisotropy terms (i.e., the terms with an ϵ_4 factor in Eq. (25)) and the anti-trapping current only when $\nabla^2\phi \geq 10^{-6}$ as these are interfacial effects only present in the vicinity of the solid-liquid interface, and is set to zero otherwise. Additionally, the first term on the right-hand side of Eq.(26), which is the solute diffusion term, is only calculated when $(1-\phi) \geq 10^{-6}$ as depicted in reference [29] as the solid-state diffusion is assumed to be negligible, and hence vanishes in the bulk solid phase.

A solid seed of radius r is defined at the bottom of the 2D computational domain, and the initial solute concentration field c in the solid and liquid phase is defined as kc_∞ and c_∞, respectively, when the solidification starts as taken in reference [25]. No flux boundary condition is set on all four sides of the 2D computational domain.

To destabilize the initial planar interface and trigger the formation of side branches at each grid point (i,j) and at each time step, a random perturbation $\eta\beta_{i,j}\sqrt{\Delta t}$ [29] is added to the value of $\phi_{i,j}$ at the next time step as:

$$\phi_{i,j}(t+\Delta t)=\phi_{i,j}(t)+\Delta t\frac{\partial\phi_{i,j}}{\partial t}+(1-\phi^2)\eta\beta_{i,j}\sqrt{\Delta t} \quad (33)$$

where $\beta_{i,j}$ is a random number with a flat distribution generated in the range [-0.5,0.5], η is the noise amplitude which is set as 0.01 [29], and Δt is the time step. The prefactor of $(1-\phi^2)$ with the perturbation keeps the noise localized in the vicinity of the interface where $\phi \neq \pm 1$. The complete programming was done in MATLAB.

2.2.3 Simulation Parameters. The parameters used for the simulation are depicted in Table 2. The value of λ is selected to be 35, which is the smallest tested value that assures the convergence of the simulation. Using this, the value of W and τ_o were calculated with the respective equations mentioned in section 2.2.1. The value of ΔX is taken to be 0.8 times the interfacial width W as taken in reference [25] to assure the capture of the interfacial phenomenon. The time step is set at $0.007\tau_o$ to assure the numerical stability for the diffusion equation in 2 dimensions for the Euler explicit scheme, which is given by the condition:

$$\Delta t < \frac{(\Delta X)^2}{4D} \quad (34)$$

Downloaded from http://asmedigitalcollection.asme.org/MSEC/proceedings-pdf/MSEC2024/88117/V002T06A008/7366697/v002t06a008-msec2024-124375.pdf by University of Michigan user on 26 January 2025

Copyright © 2024 by ASME

The slope of the liquidus line for 10 wt% Si is calculated from the phase diagram for Mg-Si alloys.

TABLE 2: SIMULATION PARAMETERS - PHASE FIELD

Input	Value	Unit
Domain	10×10	μm^2
Mesh	1118×1118	
Initial solute concentration (c_∞)	10	wt% Si
Partition coefficient (k)	0.3	
Liquid diffusion coefficient (D)	9×10^{-9}[31]	$m^2 s^{-1}$
Liquidus line slope (m)	15.83	K $(wt\%Si)^{-1}$
Gibbs Thomson coefficient (Γ)	7.46×10^{-8}[32]	mK
Anisotropy strength (ϵ_4)	0.002	
Thermal capillary length (d_o)	2.022×10^{-10}	m
Interfacial Width (W)	1.12×10^{-8}	m
Coupling constant (λ)	35	
Relaxation time (τ_o)	3.05×10^{-7}	s
Pulling Velocity (V_P)	0.05-0.1	ms^{-1}
Grid spacing (ΔX)	0.8	W
Time step (Δt)	0.007	τ_o

3. RESULTS AND DISCUSSION

3.1 Thermally Favourable Process Parameters

3.1.1 First run. As discussed in Section 2.1.5, initial tests were run by setting the melting point of Mg_2Si to 1375K at a higher solid and liquid thermal conductivity value. The parameters used for this run that are different from the ones mentioned in Table 1 are depicted in Table 3. Laser powers of 20-40W were

TABLE 3: FIRST RUN - SIMULATION PARAMETERS - CFD

Input	Value	Unit
Material melting point	1375[24]	K
Solid thermal conductivity (k_p)	7[20]	$Wm^{-1}K^{-1}$
Liquid thermal conductivity (k_l)	5[20]	$Wm^{-1}K^{-1}$
Laser diameter (R)	0.3	mm

tested with scanning speeds ranging from 0.04-0.1 ms^{-1}. The desired temperature range for this test run was set to be between 1375 K (melting point of Mg_2Si) and 1683K (melting point of Si). The maximum temperature attained in the molten pool for every tested parameter is depicted in Fig. 4.

		Laser Scanning Speed (m/s)			
		0.1	0.08	0.06	0.04
Laser Power (W)	20	1200.2 K	1270.6 K	1353.8 K	1433.3 K
	30	1468.2 K	1578.2 K	1603 K	1827.9 K
	35	1653.5 K	1690.5 K	1874.4 K	1947.6 K
	40	1723.4 K	1800.9 K	2012.1K	2368.9 K

FIGURE 4: MOLTEN POOL TEMPERATURES - FIRST RUN

The highlighted temperatures in Fig. 4 within 1375-1683K were chosen for printing the Mg_2Si powder material using the OpenAdditive PANDA SLM equipment. The printed components are depicted in Fig. 5 with a wide degree of balling, and key hole [33] effect visible as a result of the excessive Mg vaporization over the surface depending on the laser parameter and the localized melt pool temperature above its boiling point.

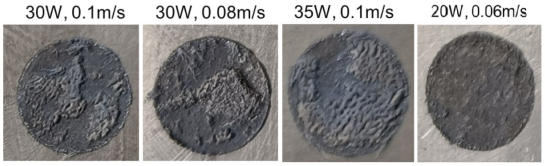

FIGURE 5: STATE OF THE PRINTED COMPONENTS (TOP VIEW)

The 20W, 0.06m/s laser configuration seems the most optimal with fewer signs of balling and porosity, signifying a minimized escape of volatile Mg, as the maximum temperature in the melt pool for this case is less than the boiling point of Mg (1363K). With 30W laser, an increase in scan rate correlates with a reduction in porosity. The Mg loss has been linked critically to the compound's stability, phase, and resulting thermoelectric properties [34**?**]. The target melt pool temperature was set close to the conventional sintering temperature. Another set of parameters was simulated and tested.

3.1.2 Second run. The sintering temperature was reduced from 1375K to 1173K (900°C), which is the reported sintering temperature in the conventional method of consolidating this material's powder[23]. Further, since the melt pool and surrounding areas of the powder bed are at a higher temperature, the corresponding solid and liquid thermal conductivity values were taken [20–22]. The complete set of parameters is depicted in Table 1. The test matrix of process parameters set for this run were laser powers of 10-15W and scanning speeds ranging from 0.05-0.2m/s. The maximum temperature attained in the molten pool for every tested parameter is depicted in Fig. 6.

The highlighted temperatures in Fig. 6 are the temperatures that fall within the temperature bounds of 1173K and 1363K, and these process parameters were hence chosen to be the most favorable parameters for fabrication. The maximum temperature obtained for the lowest scanning speed of 0.05 m/s in the 10W test was 1057.41K which is below the sintering temperature of 1173K. These parameters were tested for printing the Mg_2Si powder material. The result from the print done under processing conditions of 12.5W and 0.05 m/s is depicted in Fig. 7. which shows the x-ray diffraction pattern obtained from the precursor powder and the laser-printed sample (image of the printed sample inset). The precursor powder peaks were indexed to Mg_2Si, elemental Mg and MgO. The Mg_2Si phase in the laser-printed component is conserved to some extent with visible signs of material degradation, which has aggravated the elemental Si, and MgO content as observable from the relative intensity of the labeled peaks. Further, since the elemental Mg content is visibly unchanged (unchanged peak intensity for the Mg), it may be concluded that the reduction in the melt pool temperature successfully curtailed the Mg vaporization. Although, Mg_2Si material degradation at high temperatures in the presence of traces of oxygen is a known phenomenon [23, 35] which is observed here. As visible from Fig. 7, an intact and solid printed part without significant balling or porosity as compared to the test run has been obtained. This could be attributed to the lower melt pool temperatures attained with the refined process parameters, which are within the defined temperature bounds. Hence, it's clear that these parameters were successful in preventing the Mg

Downloaded from http://asmedigitalcollection.asme.org/MSEC/proceedings-pdf/MSEC2024/88117/V002T06A008/7366697/v002t06a008-msec2024-124375.pdf by University of Michigan user on 26 January 2025

Copyright © 2024 by ASME

		Laser Scanning Speed (m/s)						
		0.05	0.075	0.1	0.125	0.15	0.175	0.2
Laser Power (W)	10	1057.41						970.8
	12.5	1310.28	1287.92	1264.3	1169.7	1143.4	1130.2	1105.6
	15					1442.28	1439.03	1425.9

FIGURE 6: MAXIMUM TEMPERATURE IN THE MOLTEN POOL FOR DIFFERENT PROCESSING CONDITIONS - SECOND RUN

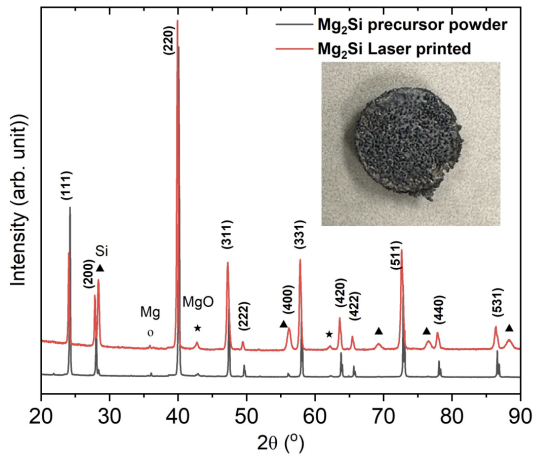

FIGURE 7: XRD COMPARISON OF THE PRECURSOR POWDER AND THE PRINTED MG2SI MATERIAL

evaporation, and a relatively denser Mg_2Si component could be obtained with laser printing, which also further validates the developed code.

3.2 Melt-Pool Thermal Kinetics

Analyzing the thermal meltpool kinetics was essential to understanding the effects of laser power and speed on the meltpool development. The meltpool temperature profiles obtained for a select set of parameters by keeping the laser power constant and increasing the scanning speed are depicted in Fig. 8. As depicted, when the scanning speed is increased by keeping the laser power constant, the peak temperature in the molten pool decreases. It can also be observed that the molten pool tail observed due to the movement of the laser becomes more prominent as the scanning speed increases.

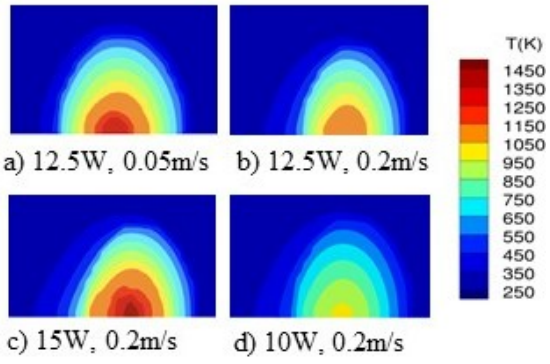

FIGURE 8: TOP VIEW OF THE MELTPOOL PROFILES WITH CHANGING PROCESS PARAMETERS

As depicted in Fig. 8, the peak temperature in the melt pool increases as expected with an increase in power, which also results in an increase in the molten pool size. The radius of the meltpool for the desired parameters was found to vary from about 20-40μm as the scanning speed decreased from 0.1 to 0.05m/s at a laser power of 12.5W. Hence, it's important to adjust the layer height and hatch spacing for each processing condition to facilitate proper adhesion between layers to fabricate these thermoelectric powders efficiently. These temperature profiles were used to calculate the temperature gradient and the cooling rate in the direction parallel to the laser path, as these parameters affect the microstructure growth and are used as input for the phase field simulation.

The temperature gradient was calculated using [36]:

$$G = \frac{T_{max} - T_l}{r} \tag{35}$$

where T_{max} is the maximum temperature in the melt pool, T_l is the liquidus temperature set as the sintering temperature in this case, and r is the distance between the location of the maximum temperature and the chosen position along the liquidus line (boundary of the melt pool). The solidification rate R can be calculated with the geometrical relationship [27]:

$$R = U_b \cos(\alpha) \tag{36}$$

where U_b is the beam scanning speed, and α is the angle between the normal to the S/L interface and the beam scanning direction. Since the temperature gradient and solidification rate are calculated in the direction parallel to the laser path in this study, α is taken as 0 degrees. The cooling rate $\dot{T}$ was calculated by taking the product of the temperature gradient G and the solidification rate R[27]:

$$\dot{T} = GR \tag{37}$$

The calculated temperature gradients and cooling rates for the three most favorable parameters are depicted below in Fig. 9. The cooling rate increases with an increase in scanning speed

Parameters	Temperature Gradient	Cooling Rate
12.5W, 0.05 m/s	1.05E+06	5.28E+04
12.5W, 0.075m/s	7.46E+05	5.60E+04
12.5W, 0.1m/s	1.04E+06	1.04E+05

FIGURE 9: CALCULATED TEMPERATURE GRADIENTS AND COOLING RATES

while the temperature gradient does not change drastically as the range of molten pool sizes and temperatures for these parameters are not very wide, as depicted in Fig. 6.

3.3 Phase Field Simulation Results

3.3.1 Code Validation. Directional solidification of dendrites is expected to happen by the edges of the molten pool[37] in the direction of the temperature gradient due to energetically

Downloaded from http://asmedigitalcollection.asme.org/MSEC/proceedings-pdf/MSEC2024/88117/V002T06A008/7366697/v002t06a008-msec2024-124375.pdf by University of Michigan user on 26 January 2025

Copyright © 2024 by ASME

favorable heterogeneous nucleation that tends to happen by the S/L interface. Since the met pool radius varies from $20\mu m$ to $40\mu m$ for this material based on the melt pool analysis, a square computational domain of size $10\mu m \times 10\mu m$ was chosen as depicted in Table. 2 to emulate the dendrite growth by the edges of the molten pool. Additionally, a small computational domain size also helped reduce the computational time.

The computational domain is initialized with a small solid nucleus with a diameter of $0.35\mu m$. Figure 10 shows the evolution of the microstructure during solidification from the pre-defined solid nucleus for a case with the laser power set to 12.5W and scanning speed set to 0.1m/s. As the solidification time increased, it can be seen that the dendrites branched out into the molten pool along the applied temperature gradient in the X direction, as depicted in Fig. 10. It can be noted that, with the passage of time, the dendrites branch out from the primary dendrites to form secondary and tertiary dendrites. And, the solute concentration ratio, as shown in Fig. 11, also follows the expected trend. The solute concentration ratio is defined as:

$$ConcentrationRatio = \frac{c}{{c_l}^o} \tag{38}$$

where ${c_l}^o$ is $\frac{c_\infty}{k}$. The concentration c of the completely solidified phase (region with ϕ = 1 in Fig. 10) and the liquid phase (region with ϕ = -1 in Fig. 10) ahead of the interface should be unchanged at the initial solute concentration of c_∞[38] which makes the concentration ratio in these regions equal to k(k = 0.3 as shown in Table 2). This aligns well with the modeling result as shown in Fig. 11. It should also be noted in Fig. 11 that the solute concentration is high in the interdendritic region as the solute is ejected from the advancing solid interface to the liquid owing to the solid's lower solute solubility compared to the liquid [38].

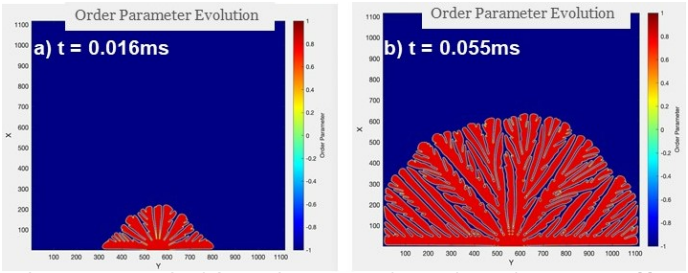

FIGURE 10: MICROSTRUCTURE EVOLUTION - Q = 12.5W, U_b = 0.1M/S

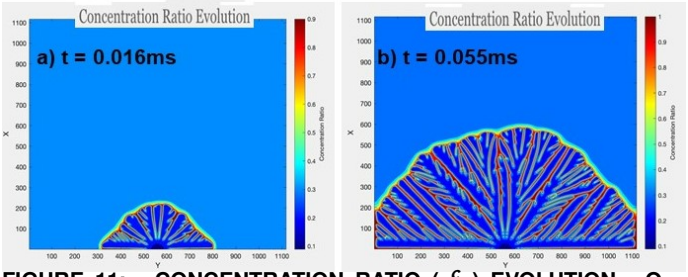

FIGURE 11: CONCENTRATION RATIO ($\frac{c}{{c_l}^o}$) EVOLUTION - Q = 12.5W, U_b = 0.1M/S

According to the theory of solidification, the concentration c ahead of the interface is high at c_∞/k and decays down to c_∞ as we move into the liquid farther away from the interface [38], which can be observed in the modeled results as seen in Fig.11.

Additionally, the Secondary Dendritic Arm Spacing (SDAS) was measured and compared with the analytical values. The analytical SDAS was calculated with the analytical model proposed by Kurz and Fisher [39] as given below:

$$\lambda = 4.3(k\Delta T_o D\Gamma)^{\frac{1}{4}} R^{\frac{-1}{4}} G^{\frac{-1}{2}} \tag{39}$$

where λ is the SDAS in μm, k is the partition coefficient, ΔT_o = $|m|c_\infty(1-k)/k$, Γ is the Gibbs Thomson coefficient (Kmm), D is the diffusion coefficient (mm^2s^{-1}), R is the solidification rate (mms^{-1}), and G is the temperature gradient (K/mm). ImageJ was used to measure SDAS from the simulated result for the case depicted in Fig. 10. The average value of SDAS obtained from the simulated results was $0.012 \pm 0.0015\ \mu m$ while the analytical value obtained was approximately equal to $0.00457\ \mu m$. The variation observed can most likely be attributed to the simulation parameters like the low Gibbs-Thomson coefficient value approximated for the material[32], which is still not available in the literature and needs further research. Nevertheless, the values are still comparable, and that further validates the code.

3.3.2 Microstructural Analysis. The temperature gradient and solidification rate obtained from the CFD-based simulation for the favorable process parameters were used as input parameters in the phase field model to understand the correlation between the process parameters and the microstructure. The temperature gradient and the solidification rate corresponding to the scanning speeds of 0.05m/s and 0.1m/s at a laser power of 12.5W were used to understand the influence of increasing scanning speed on the microstructure. The results from this run after 0.038ms are depicted in Fig. 12. It can be observed that, with the increase in scanning speed (also an increase in cooling rate), there is a visible reduction in the dendrite tip radius due to increased branching near the tips. There is also a reduction in secondary and tertiary dendrite branching from the sides of the primary dendrite axes, which reduces the primary interdendritic spacing (PDAS). The average PDAS was calculated using ImageJ, and with an increase in scanning speed, the PDAS was found to reduce from 0.458 μm to 0.348 μm. Hence, the simulated microstructure follows the general rule of finer microstructure (lower PDAS) with an increase in scanning speed and cooling rate.

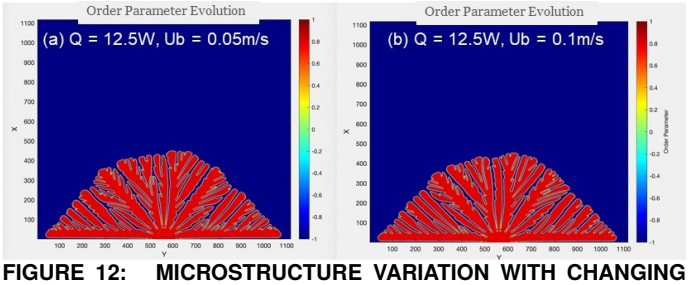

FIGURE 12: MICROSTRUCTURE VARIATION WITH CHANGING SCANNING SPEED (T=0.038MS)

The interdendritic regions are solute-rich, as depicted in Fig. 11, and these are the regions that solidify in the end. Hence, an

Downloaded from http://asmedigitalcollection.asme.org/MSEC/proceedings-pdf/MSEC2024/88117/V002T06A008/7366697/v002t06a008-msec2024-124375.pdf by University of Michigan user on 26 January 2025

Copyright © 2024 by ASME

increase in the fraction of interdendritic regions would decrease the compositional and phase homogeneity of the material, which could alter the electrical and thermal carrier transport of Mg_2Si resulting in alteration of its thermoelectric properties. This correlation requires more experimental data for validation with the microstructural and phase analysis with respect to the thermoelectric properties. As discussed in this section, the processing parameters can be optimized to enable efficient SLM fabrication of thermoelectric powders.

4. CONCLUSION

Fabrication of the Mg_2Si using SLM is demonstrated along with the process's numerical CFD analysis. A three-dimensional numerical model of the molten pool was developed, with varying laser powers and scanning speeds to derive temperature profiles and process parameters. The range in which the melt pool temperature lies with respect to the boiling point of Mg was found to be crucial to preserve the phase and structural integrity of the printed component.

Further, the thermal data from the CFD model was input to a phase field analysis aimed at understanding the impact of processing parameters on dendritic growth during solidification. The effect of increasing the laser scanning speed, hence a higher cooling rate, was observed to result in a finer microstructure with reduced Primary Dendrite Arm Spacing (PDAS). Thus, tailoring the microstructure is possible to suit the application.

Furthermore, the study opens the scope for an extensive material characterization of the fabricated Mg_2Si components. This would entail a thorough examination of the microstructure and functional properties to understand how the various processing conditions influence it and how accurately it fits with the phase field modeled data.

ACKNOWLEDGMENTS

The authors gratefully acknowledge financial support from the National Science Foundation (NSF) via Grant #2244686.

APPENDIX A. NOMENCLATURE

ρ Density [kg m^{-3}]
Ub Laser beam velocity [ms^{-1}]
c_p Specific heat [$J/K.kg$]
μ^* Effective viscosity [kg $(ms)^{-1}$]
T Temperature [K]
t Time [s]
g Acceleration due to gravity [ms^{-2}]
k^* Effective thermal conductivity [W/mK]
S_h Energy source term [Wm^{-3}]
ϵ Porosity
T_M Material sintering temperature [K]
H, h Enthalpy [J/kg]
f_s, f_l Solid and liquid mass fraction
k_l Liquid thermal conductivity [W/mK]
u, v, w Velocities in x,y, and z directions [m s^{-1}]
μ_s, μ_l Solid and liquid viscosity [kg $(ms)^{-1}$]
U Dimensionless supersaturation
c Solute concentration[$wt\%Si$]
l Thermal length[m]
L Latent heat [J/kg]
β_T Thermal expansion coefficient [K^{-1}]
β_s Solute expansion coefficient [K^{-1}]
T_a Ambient temperature [K]
θ Energy absorption coefficient
ϵ_b Emissivity
h_c Convective heat transfer coefficient [$Wm^{-2}K^{-1}$]
R Laser diameter [m]
σ_b Boltzmann constant [$Wm^{-2}K^{-4}$]
q_o Laser intensity [Wm^{-2}]
D Liquid diffusion coefficient[m^2s^{-1}]
σ_s Surface tension [Nm^{-1}]
ψ Limiter function
a_E, a_W, a_N, a_S, a_F, a_B, a_P TVD coefficients
$F_e, F_w, F_n, F_s, F_f, F_b$ Convective mass flux [kg/m^2s]
S_u^{DC} Deferred correction source term
G Temperature gradient[K/m]
R Solidification rate[m/s]
T Cooling rate[K/s]
r Ratio of gradients
$c\infty$ Initial solute concentration[$wt\%Si$]
k Partition coefficient
D Liquid diffusion coefficient[m^2s^{-1}]
m Liquidus line slope [$K(wt\%Si)^{-1}$]
Γ Gibbs Thomson coefficient[mK]
ϵ_4 Anisotropy strength
d_o Thermal capillary length[m]
W Interfacial width[m]
λ Coupling constant
τ_o Relaxation time[s]
V_P Pulling velocity[ms^{-1}]
ΔX Grid spacing[W]
Δt Time step[τo]
v_s, v_n Velocity parallel and perpendicular to the surface [ms^{-1}]
ϕ Phase field order parameter
$\bar{}D$ Dimensionless diffusion coefficient
$\bar{}V_P$ Dimensionless pulling velocity
$\bar{}l_T$ Dimensionless thermal length

REFERENCES

[1] Razvan, Pacurar and Ancuta, Pacurar. "Applications of the Selective Laser Melting Technology in the Industrial and Medical Fields." Shishkovsky, I. V. (ed.). *New Trends in 3D Printing*. IntechOpen, Rijeka (2016), Chap. 8. DOI 10.5772/63038.

[2] Thimont, Y. and Leblanc, S. "The impact of thermoelectric leg geometries on thermal resistance and power output." *Journal of Applied Physics* Vol. 126 (2019): p. 095101. DOI 10.1063/1.5115044.

[3] Goyal, G.K. and Dasgupta, T. "Fabrication and testing of Mg2Si1-xSnx based thermoelectric generator module." *Materials Science and Engineering: B* Vol. 272 (2021): p. 115338. DOI https://doi.org/10.1016/j.mseb.2021.115338.

[4] Goyal, G.K. and Dasgupta, T. "Generic Approach for Contacting Thermoelectric Solid Solutions: Case Study in n- and p-Type Mg2Si0.3Sn0.7." *ACS applied materials interfaces* Vol. 13 (2021). DOI 10.1021/acsami.0c19485.

[5] Camut, J., Ziolkowski, P., Ponnusamy, P., Stiewe, C., Mueller, E. and deBoor, J. "Efficiency Measurement and Modeling of a High-Performance Mg2(Si,Sn)-Based Thermoelectric Generator." *Advanced Engineering Materials* Vol. 25 No. 1 : p. 2200776. DOI https://doi.org/10.1002/adem.202200776.

[6] Zhang, B., Zuo, L., Fu, G., Shi, X., Tewolde, M., Longtin, J., Chen, Y. and Sampath, S. "Thermoelectric Properties of Magnesium Silicide Prepared by Thermal Spraying." 2012. DOI 10.1115/HT2012-58453.

[7] Li, C., Wu, Y. and Liu, X. "Morphological evolution and growth mechanism of primary Mg 2Si phase in Al–Mg 2Si alloys." *Acta Materialia - ACTA MATER* Vol. 59 (2011): pp. 1058–1067. DOI 10.1016/j.actamat.2010.10.036.

[8] Xiao, B. and Zhang, Y. "Marangoni and Buoyancy Effects on Direct Metal Laser Sintering with a Moving Laser Beam." *Numerical Heat Transfer Part A-applications - NUMER HEAT TRANSFER PT A-APPL* Vol. 51 (2007): pp. 715–733. DOI 10.1080/10407780600968593.

[9] Wu, Y., Sun, K., Yu, S. and Zuo, L. "Modeling the selective laser melting-based additive manufacturing of thermoelectric powders." *Additive Manufacturing* Vol. 37 (2021): p. 101666. DOI https://doi.org/10.1016/j.addma.2020.101666.

[10] Bing-hui, T., Meng-wu, W., Ang, Z., Zhipeng, G. and Shoumei, X. "Phase-field modeling of dendritic growth of magnesium alloys with a parallel-adaptive mesh refinement algorithm." *China Foundry* Vol. 18 (2021): pp. 541 – 549.

[11] Wang, F., Matz, A., Tschukin, O., Heimann, J., Matz, Bettina, M., Nestler, Britta and Jost, Norbert. "Numerical and Experimental Investigations on the Growth of the Intermetallic Mg 2 Si Phase in Mg Infiltrated Si-Foams: Numerical and Experimental Investigations on the Growth. . . ." *Advanced Engineering Materials* Vol. 19 (2017): p. 1700063. DOI 10.1002/adem.201700063.

[12] Voller, V.R., Brent, A.D. and Prakash, C. "The modelling of heat, mass and solute transport in solidification systems." *International Journal of Heat and Mass Transfer* Vol. 32 No. 9 (1989): pp. 1719–1731. DOI https://doi.org/10.1016/0017-9310(89)90054-9.

[13] Z, Radyadour Kh. "Joseph Boussinesq and his approximation: a contemporary view." *Comptes Rendus Mécanique* Vol. 331 No. 8 (2003): pp. 575–586. DOI https://doi.org/10.1016/S1631-0721(03)00120-7.

Downloaded from http://asmedigitalcollection.asme.org/MSEC/proceedings-pdf/MSEC2024/88117/V002T06A008/7366697/v002t06a008-msec2024-124375.pdf by University of Michigan user on 26 January 2025

Copyright © 2024 by ASME

[14] Hadley, G.R. "Thermal conductivity of packed metal powders." *International Journal of Heat and Mass Transfer* Vol. 29 No. 6 (1986): pp. 909–920. DOI https://doi.org/10.1016/0017-9310(86)90186-9.

[15] Carter, M., El-Desouky, A., Andre, M., Bardet, P. and Leblanc, S. "Pulsed laser melting of bismuth telluride thermoelectric materials." *Journal of Manufacturing Processes* Vol. 43 (2019): pp. 35–46. DOI 10.1016/j.jmapro.2019.04.021.

[16] Wang, S.K. "Weld Pool Convection and Its Effect." 2013. URL https://api.semanticscholar.org/CorpusID:214661524.

[17] Patankar, S. V. *Numerical heat transfer and fluid flow*. Series on Computational Methods in Mechanics and Thermal Science, Hemisphere Publishing Corporation (CRC Press, Taylor & Francis Group) (1980).

[18] van Leer, B. "Towards the Ultimate Conservative Difference Scheme. II. Monotonicity and Conservation Combined in a Second-order Scheme." *Journal of Computational Physics* Vol. 14 (1974): pp. 361–370. DOI 10.1016/0021-9991(74)90019-9.

[19] Versteeg, H. K. and Malalasekera, W. *An introduction to computational fluid dynamics - the finite volume method.* Addison-Wesley-Longman (1995).

[20] Akasaka, M., Iida, T., Matsumoto, A., Yamanaka, K., Takanashi, Y., Imai, T. and Hamada, N. "The thermoelectric properties of bulk crystalline n- and p-type Mg2Si prepared by the vertical Bridgman method." *Journal of Applied Physics* Vol. 104 (2008): pp. 013703 – 013703. DOI 10.1063/1.2946722.

[21] Richard, J. L. and Donald, R. M. "The Thermal Conductivities of Mg2Si and Mg2Ge." *Journal of The Electrochemical Society* Vol. 110 No. 2 (1963): p. 121. DOI 10.1149/1.2425688.

[22] Satyala, N. and Vashaee, D. "Modeling of Thermoelectric Properties of Magnesium Silicide (Mg 2 Si)." *Journal of Electronic Materials* Vol. 41 (2012): pp. 1785–1791. DOI 10.1007/s11664-012-2024-7.

[23] Mitra, K., Goyal, G.K., Rathore, E., Biswas, K., Vitta, S., Mahapatra, S. and Dasgupta, T. "Enhanced Thermoelectric Performance in Mg 2 Si by Functionalized Co-Doping." *physica status solidi (a)* Vol. 215 (2018): p. 1700829. DOI 10.1002/pssa.201700829.

[24] B, Yu., Chen, D., Q., Tang, Wang, C. and Shi, D. "Structural, electronic, elastic and thermal properties of Mg2Si." *Journal of Physics and Chemistry of Solids* Vol. 71 (2010): pp. 758–763.

[25] Echebarria, B., Folch, R., Karma, A. and Plapp, M. "Quantitative Phase Field Model of Alloy Solidification." *Physical review. E, Statistical, nonlinear, and soft matter physics* Vol. 70 (2005): p. 061604. DOI 10.1103/PhysRevE.70.061604.

[26] Karma, A. "Phase-Field Formulation for Quantitative Modeling of Alloy Solidification." *Phys. Rev. Lett.* Vol. 87 (2001): p. 115701. DOI 10.1103/PhysRevLett.87.115701.

[27] Wang, X. and Chou, K. "Microstructure simulations of Inconel 718 during selective laser melting using a phase field model." *The International Journal of Advanced Manufacturing Technology* Vol. 100 (2019). DOI 10.1007/s00170-018-2814-z.

[28] Provatas, Nikolas and Elder, Ken R. "Phase-Field Methods in Materials Science and Engineering." 2010.

[29] Tourret, D. and Karma, A. "Growth competition of columnar dendritic grains: A phase-field study." *Acta Materialia* Vol. 82 (2015): pp. 64–83. DOI https://doi.org/10.1016/j.actamat.2014.08.049.

[30] Xiao, W., Li, S., Wang, C., Shi, Y., Mazumder, J., Xing, H. and Song, L. "Multi-scale simulation of dendrite growth for direct energy deposition of nickel-based superalloys." *Materials Design* Vol. 164 (2018): p. 107553. DOI 10.1016/j.matdes.2018.107553.

[31] Qin, J., Li, X., Wang, J. and Pan, S. "The self-diffusion coefficients of liquid binary M-Si (M=Al, Fe, Mg and Au) alloy systems by first principles molecular dynamics simulation." *AIP Advances* Vol. 9 (2019): p. 035328. DOI 10.1063/1.5067295.

[32] Kahveci, O., Erol, H., Joban, O. and Gündüz, M. "Determination of solid-liquid interfacial energy of solid Mg2Si intermetallic phase in equilibrium with liquid Al-SiMg eutectic solution in AlSiMg energy storage alloy." *Intermetallics* Vol. 135 (2021): p. 107235. DOI 10.1016/j.intermet.2021.107235.

[33] Liu, S. and Guo, H. "Balling Behavior of Selective Laser Melting (SLM) Magnesium Alloy." *Materials* Vol. 13 (2020): p. 3632. DOI 10.3390/ma13163632.

[34] Goyal, G. K. and Dasgupta, T. "Effect of Magnesium Content and Processing Conditions on Phase Formation and Stability in Mg2+Si0.3Sn0.7." *Journal of Electronic Materials* Vol. 47 (2018). DOI 10.1007/s11664-017-6012-9.

[35] Gunstein, S., Alexander, B., Alexander, S., Reidar, H. and Hugh, M. "High temperature oxidation of Mg2(Si-Sn)." *Corrosion Science* Vol. 111 (2016): pp. 325–333. DOI https://doi.org/10.1016/j.corsci.2016.05.016.

[36] Sahoo, s. and Chou, K. "Phase-field simulation of microstructure evolution of Ti–6Al–4V in electron beam additive manufacturing process." *Additive Manufacturing* Vol. 9 (2016): pp. 14–24. DOI https://doi.org/10.1016/j.addma.2015.12.005.

[37] Yefeng, Y., Lu, W., Jun, Z., Hongxin, L., Yang, L., Wentao, Y. and Feng, L. "Impact of fluid flow on the dendrite growth and the formation of new grains in additive manufacturing." *Additive Manufacturing* Vol. 55 (2022): p. 102832. DOI https://doi.org/10.1016/j.addma.2022.102832.

[38] Davis, S. H. *Theory of Solidification*. Cambridge Monographs on Mechanics, Cambridge University Press (2001). DOI 10.1017/CBO9780511546747.

[39] Kurz, W. and Fisher, D.J. "Dendrite growth at the limit of stability: tip radius and spacing." *Acta Metallurgica* Vol. 29 No. 1 (1981): pp. 11–20. DOI https://doi.org/10.1016/0001-6160(81)90082-1.

[40] Hengji, Z., Zheng, T., Gnade, B. and Cho, K. "The effect of point defects and nanoparticles on thermal conductivity of magnesium silicide." *Computational Materials Science* Vol. 104 (2015). DOI 10.1016/j.commatsci.2015.03.014.

Downloaded from http://asmedigitalcollection.asme.org/MSEC/proceedings-pdf/MSEC2024/88117/V002T06A008/7366697/v002t06a008-msec2024-124375.pdf by University of Michigan user on 26 January 2025

Copyright © 2024 by ASME